HELIOCENTRIC ESCAPE AND LUNAR IMPACT FROM NEAR RECTILINEAR HALO ORBITS

Diane C. Davis,[*] Kenza K. Boudad,[†] Rolfe J. Power,[‡] and Kathleen C. Howell[§]

Spacecraft departing from the Gateway in a Near Rectilinear Halo Orbit (NRHO) experience gravitational forces from the Moon, the Earth, and the Sun, all of which can be simultaneously significant. These complex dynamics influence the eventual destinations of the departing spacecraft. The current investigation examines the flow of objects leaving NRHOs in the Bicircular Restricted Four-Body Problem, and results are applied to heliocentric escape and lunar impact trajectories in a higher-fidelity ephemeris model. Separation maneuver magnitude, direction, and location are correlated with successful departure to various destinations via maps and specific examples.

INTRODUCTION

The Gateway[1] is proposed as a crewed outpost supporting a variety of exploration missions. As a staging ground for lunar surface missions and for exploration beyond cislunar space, the Gateway will experience spacecraft periodically arriving and docking, and subsequently, spacecraft and objects with a wide range of shapes and masses will also depart the Gateway for other destinations. Notable examples of Gateway departures include lander descent to the lunar surface, safe disposal of discarded logistics modules or ascent elements to heliocentric space, and deployment of cubesats to various locations in cislunar space. Each departure is governed by the dynamics of the Gateway orbit and the surrounding dynamical environment. The current baseline orbit for the Gateway is a Near Rectilinear Halo Orbit (NRHO) near the Moon.[2] NRHOs exhibit nearly stable behavior, but over time, any unmaintained object in such an orbit eventually departs due to the small instabilities associated with these NRHOs. A separation maneuver speeds the departure from the NRHO, but the effects of the maneuver on the spacecraft behavior depend on the location, magnitude, and direction of the burn. The departing flow changes significantly based on these burn parameters, resulting in a large design space. Employing maps and other visualizations aids in condensing the potential departure options. The maps and visuals enable a broad understanding of the design space and identification of particular trajectories that lead to desired behavior; broad regions of the separation maneuver space are also excluded as undesirable.

Previous investigations[3,4] examined departure from the NRHO and escape from the Earth-Moon vicinity from the perspective of logistics module (LM) disposal. The current investigation extends this work, exploring several additional aspects of the departure dynamics from the NRHO. First, the bicircular restricted 4-body problem (BCR4BP) is employed to characterize the natural flow of trajectories departing the NRHO. Then, maneuvers that result in escape to heliocentric space are explored. Groups of separation burns that

---

[*] Principal Systems Engineer, a.i. solutions, Inc., 2224 Bay Area Blvd, Houston TX 77058, diane.davis@ai-solutions.com.

[†] Ph.D. Student, School of Aeronautics and Astronautics, Purdue University, Armstrong Hall of Engineering, 701 W. Stadium Ave., West Lafayette, IN 47907-2045, kboudad@purdue.edu.

[‡] Graduate Student, School of Aeronautics and Astronautics, Purdue University, Armstrong Hall of Engineering, 701 W. Stadium Ave., West Lafayette, IN 47907-2045, rpower@purdue.edu.

[§§] Hsu Lo Distinguished Professor, School of Aeronautics and Astronautics, Purdue University, Armstrong Hall of Engineering, 701 W. Stadium Ave., West Lafayette, IN 47907-2045, howell@purdue.edu. Fellow AAS; Fellow AIAA.

yield sufficient energy to escape the Earth-Moon vicinity are identified through Hamiltonian maps, and then maneuver orientations that allow solar gravity to pull a departing spacecraft into heliocentric space are determined. Finally, lunar impact trajectories originating from the NRHO are explored.

DYNAMICAL MODELS

In this investigation, three dynamical models are employed. The CR3BP[5] provides a framework for investigation of departure dynamics and flow nearby the NRHO before and immediately after separation from the Gateway, including lunar impact trajectories. In this regime, the primary gravitational influences on the spacecraft are the Earth and Moon, and the CR3BP is an effective approximation for the dynamics. As the spacecraft departs the immediate vicinity of the NRHO near the Moon, the effects of the Sun become significant. Thus, the BCR4BP[6] is employed to characterize the behavior of a departing spacecraft. The BCR4BP incorporates the influence of solar gravity on the Earth-Moon-spacecraft three-body system and offers an increase in fidelity over the CR3BP, while still offering insight into the underlying dynamical behavior in the system. Finally, an N-body model based on ephemeris data provides higher-fidelity analysis for particular mission scenarios.

The Circular Restricted 3-Body Problem

The CR3BP describes the motion of a massless spacecraft affected by two primary gravitational bodies such as the Earth and the Moon. The model assumes that the two primary bodies are point masses orbiting their center of mass in circular orbits. The spacecraft moves freely under the influence of the two primaries, and its motion is described relative to a rotating reference frame. No closed-form solution exists to the CR3BP equations of motion, but five equilibrium solutions, the libration points, are denoted L_1 through L_5. Stable and unstable periodic orbit families, including the L_2 halo orbits, emerge in the vicinity of the libration points. A single integral of the motion exists in the CR3BP, the Jacobi constant,[5] written

$$J = 2U^* - v^2 \tag{1}$$

where v is the rotating velocity magnitude. The pseudopotential U^* is a function only of position, defined as

$$U^* = \frac{1}{2}(x^2 + y^2) + \frac{\mu}{r} + \frac{(1-\mu)}{d} \tag{2}$$

where x, y, and z are components of the position vector relative to the barycenter in the Earth-Moon rotating frame and $\dot{x}, \dot{y}$, and $\dot{z}$ are components of the velocity vector in the same frame. The values d and r are the distances between the spacecraft and P_1 and P_2 respectively, and $\mu = \frac{m_2}{m_1 + m_2}$ is the mass parameter of the system where m_1 and m_2 are the masses of the two primaries. An energy-like quantity, the Jacobi constant limits the motion of the spacecraft to regions in space where $v^2 > 0$, with zero velocity surfaces (ZVSs) bounding the regions within which the spacecraft can move freely. For values of Jacobi constant greater than that associated with the L_1 libration point, the ZVSs form closed regions around each of the two primaries. As the energy of the spacecraft trajectory increases, the value of Jacobi constant decreases until, at the L_1 value, the ZVSs open at the L_1 libration point and the spacecraft can move between the two primaries. Similarly, when the value of the Jacobi constant decreases to the value associated with L_2, the ZVSs open at L_2 and the spacecraft is able to escape the vicinity of the primaries entirely. For spacecraft orbiting in one of the selected NRHOs, the CR3BP is a good approximation for the behavior of the trajectory.

The Bicircular Restricted 4-Body Problem

In scenarios where the gravitational influence of the Sun is non-negligible, a higher-fidelity model is necessary to accurately describe the spacecraft behavior. The BCR4BP incorporates the gravitational effects of three massive bodies, for instance, the Earth, the Moon and the Sun, on the motion of a spacecraft.[7] The mass of the spacecraft is assumed to be negligible in comparison to the
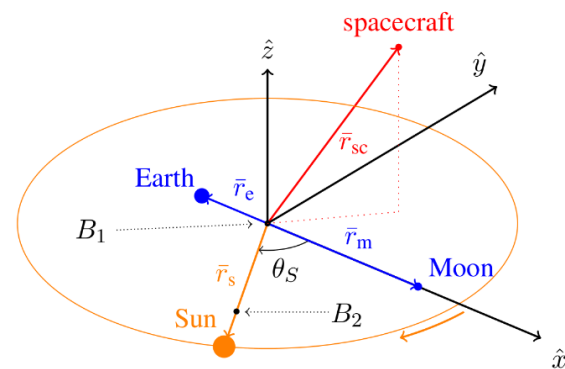

Figure 1. BCR4BP in the Earth-Moon rotating frame

masses of the other bodies. In this model, the Earth and the Moon are assumed to move in circular orbits around their common barycenter, denoted B_1, while the Sun and B_1 move in circular orbits with respect to the Earth-Moon-Sun barycenter, labeled B_2, as denoted in Figure 1. The BCR4BP is not a coherent model: the perturbing acceleration from the Sun does not influence the motion of the Earth and the Moon, thus, the motion of the Moon is not a solution to the Sun-Earth CR3BP. The equations of the motion in the CR3BP are extended to include the solar gravitational influence as follows,

$$\ddot{x} = 2\,\dot{y} + \frac{\partial \Upsilon^*}{\partial x}, \quad \ddot{y} = -2\,\dot{x} + \frac{\partial \Upsilon^*}{\partial y}, \quad \ddot{z} = \frac{\partial \Upsilon^*}{\partial z} \tag{2}$$

where

$$\Upsilon^* = U^* + \frac{m}{r_{s\,s/c}} - \frac{m}{a^3}\left(\bar{r}_s \cdot \bar{r}_{s/c}\right), \tag{3}$$

$m = \frac{m_S}{m_e + m_m}$ is the nondimensional mass of the Sun, and $a = \frac{r_s}{r_{em}}$ is the nondimensional distance between the Earth-Moon barycenter and the Sun. The independent time variable, t, explicitly appears in the BCR4BP pseudo-potential. Therefore, the BCR4BP is time-dependent and does not admit an integral of the motion. However, a scaled version of the Hamiltonian is defined to be consistent with the Jacobi constant in the CR3BP, i.e.,

$$H(\theta) = 2\Upsilon^* - \sqrt{\dot{x}^2 + \dot{y}^2 + \dot{z}^2} \tag{4}$$

The time-dependent nature of the differential equations in the BCR4BP yields time-dependent equilibrium solutions. These instantaneous equilibrium solutions correspond to the perturbed, or oscillating, CR3BP libration points (L_i), and are denoted $E_1(\theta_s)$ through $E_5(\theta_s)$. Similarly, time-dependent ZVSs in the BCR4BP define instantaneous forbidden regions for a given value of H. Note that the relative positions of the primaries in the BCR4BP are periodic: one period corresponds to the time between consecutive alignments of the Earth, the Moon and the Sun (in this order) and is approximately equal to 29.5 days, i.e., one synodic period.

The N-Body Ephemeris Model

For applications in mission scenarios where high-fidelity modeling accuracy is required, N-body differential equations and planetary ephemerides are employed. The N-body dynamics describe the motion of a particle of interest (e.g., a spacecraft) in an inertial frame relative to a central body under the gravitational influence of the same central body and additional perturbing bodies. Within this analysis, the relative position of each perturbing body with respect to the central body is instantaneously computed by employing NAIF SPICE ephemeris data. The Moon is selected as the central body for numerical integration in the J2000 inertial frame. The Earth and Sun are included as point masses, and the Moon's gravity is modeled using the GRAIL (GRGM660PRIM) model truncated to degree and order 8. Solar radiation pressure (SRP) acting on a sphere is also included in the force model.

For multi-revolution propagations in the NRHO prior to a disposal maneuver, orbit maintenance maneuvers (OM maneuvers) are implemented. In some simulations, operational errors on the spacecraft are considered in the higher-fidelity modeling. In these simulations, each OM maneuver is associated with a navigation error on the spacecraft state: both low navigation errors of 1 km in position and 1 cm/s in velocity and larger navigation errors of 10 km in position and 10 cm/s in velocity are considered. Maneuver execution errors comprising 1.5% in magnitude and 1° in direction, as well as a fixed magnitude of 1.42 mm/s, are applied to each OM maneuver. Mismodeling in SRP assumptions provide 15% error in area and 30% error in coefficient of reflectivity. Momentum wheel desaturations are assumed to occur once per revolution near apolune with a translational Δv component of 3 cm/s applied in a random direction. In addition, the disposal maneuver is applied with a 1.5% execution error in magnitude with lower or higher navigation errors on the state, as specified in each case. All values are 3σ and are implemented as Gaussian errors with zero mean.

REFERENCE NRHOs AND DEPARTURE

The current analysis focuses on two NRHOs. The reference orbit for the Gateway spacecraft is a southern L_2 NRHO in a 9:2 resonance with the lunar synodic period; that is, the spacecraft completes nine revolutions within the NRHO in the time it takes the Sun-Earth-Moon geometry to repeat twice. With a perilune radius of approximately 3,250 km and an apolune radius of about 71,000 km, a spacecraft in the 9:2 NRHO completes one revolution about every 6.5 days. The second NRHO of interest is a southern L_2 NRHO in a

4:1 resonance with the lunar synodic period. With a longer period of about 7.3 days, the 4:1 NRHO passes farther from the Moon with a perilune radius of approximately 5,750 km and an apolune radius of about 75,000 km. Perfectly periodic in the CR3BP, the two NRHOs retain their periodicity in the BCR4BP,[8] but they become quasi-periodic orbits in the higher-fidelity ephemeris force model. In any of the three models, the NRHOs are nearly stable. The maximum stability indices[9] associated with the 9:2 and 4:1 NRHOs in the CR3BP have magnitudes equal to about 1.3 and 1.6 respectively, where a maximum stability of index of 1 represents a marginally stable orbit in a linear analysis. In contrast, the maximum stability index in the L_2 halo family reaches a value of over 600 where the family bifurcates from the L_2 Lyapunov orbit family. While the 9:2 and 4:1 NRHOs are nearly stable, over time perturbations cause an object to depart if the orbit is not maintained. Departure from the NRHO is assessed based on a momentum integral.[10] The momentum integral, MI, is a line integral of the position vector from the initial time, t_0, to the current time, t,

$$\text{MI}(t) = \int_{t_0}^{t} x(\tau)\dot{x}(\tau) + y(\tau)\dot{y}(\tau) + z(\tau)\dot{z}(\tau)d\tau \qquad (4)$$

For a perfectly periodic halo orbit in the CR3BP and BCR4BP, the MI is also periodic and returns to zero after precisely one period. In the higher-fidelity ephemeris model, the value of the MI does not return precisely to zero over one period, however, it does remain bounded while the spacecraft remains in the NRHO. Over time, as the orbit of a perturbed or unmaintained spacecraft diverges from the NRHO, the magnitude of the MI also increases, and departure is defined in terms of the divergence of the MI. In the current analysis, when the magnitude of the MI crosses a threshold of 0.1, the debris object is considered 'departed' from the NRHO. Since the stability index of the 9:2 NRHO is greater than one, an object moving along the NRHO will depart without orbit maintenance. In the CR3BP, depending on the convergence tolerance and numerical integration techniques, a departure from the 9:2 NRHO without a maneuver occurs after about 230 days. In the higher-fidelity ephemeris model, departure times without a separation maneuver or orbit maintenance range from 70 - 100 days for a quiet, uncrewed spacecraft to 30-60 days for a noisy, crewed configuration. When a separation maneuver is applied to an object departing the Gateway, departure time decreases. A previous investigation[4] characterizes time to depart as a function of maneuver magnitude and true anomaly for maneuvers in the velocity, normal, and binormal directions in the CR3BP. The fastest observed departures occur after separation burns in the velocity direction at perilune. Such maneuvers are further explored in the ephemeris force model. For velocity-direction separation maneuvers at perilune, certain maneuver magnitudes lead to consistent times to depart across all revolutions in both the 9:2 and 4:1 NRHOs, while other maneuver magnitudes result in variable departure times from one revolution to the next.

FLOW ANALYSIS IN THE BICIRCULAR RESTRICTED FOUR-BODY PROBLEM

Once an object has departed from the NRHO, its ultimate destination depends on the departing flow. Two models are used to explore the departing behavior. While an object remains in or near the NRHO, the CR3BP effectively describes its behavior. Once the object has departed, solar gravity has a significant effect on the trajectory, and the BCR4BP is employed for higher-fidelity analysis.

First, information about the departure dynamics from the NRHO is investigated using dynamical systems theory and the Earth-Moon CR3BP. Although described as 'nearly stable' orbits, NRHOs in a 9:2 resonance and a 4:1 resonance with the lunar synodic period possess a saddle mode, as apparent in Table 1 and, thus, stable and unstable manifolds. The six-dimensional angle between the stable and unstable eigenvectors along a revolution of the 9:2 synodic resonant NRHO appears in Figure 2. Near apolune, the eigenvectors are oriented in distinct directions, and the angle reaches a maximum value of 53 degrees. Close to the Moon, however, the angle between the stable and unstable eigenvectors is small, with a minimum value of less than 4 degrees at perilune. The small angle indicates that the eigenvectors (and, thus, manifolds) are not well defined near perilune; for example, a step along the unstable eigenvector can result in a propagated step close to the unstable manifold, a step near the stable manifold, or a combination of both modes. The proximity of the eigenvector spaces represents an additional challenge in the near vicinity of the Moon, along with strong nonlinear effects and numerical challenges.

Table 1. Stability quantities associated with the CR3BP 4:1 and the 9:2 NRHOs.

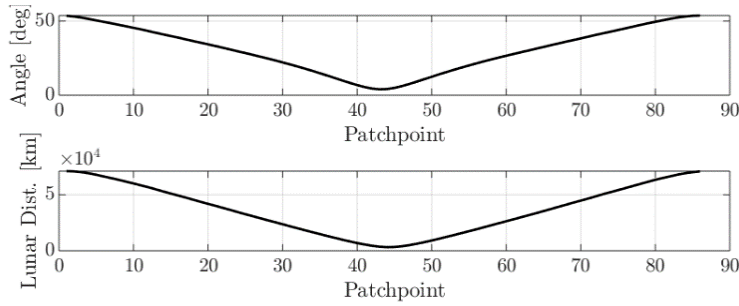| Orbit	Eigenvalues			Stability indices		
4:1 NRHO	1,	$0.5067 - 0.8621i,$	-2.9027	1,	$0.5067,$	-1.6236
9:2 NRHO	1,	$0.6846 + 0.7289i,$	-2.1774	1,	$0.6846,$	-1.3183

Figure 2. Angle between unstable and stable eigenvectors of the 9:2 NRHO

The baseline 9:2 NRHO is discretized and patch points are selected where the eigenvectors are the most distinct, that is, near apolune, as depicted in Figure 3a. A step along the unstable eigenvector is computed, and the resulting state is propagated in the Earth-Moon CR3BP. Trajectories along the unstable manifold for initial states post-apolune appear in Figures 3b and 3c, while trajectories for initial states prior to apolune appear in Figures 3d and 3e. The geometries are consistent with departure/disposal trajectories observed previously:[3,4] excursions to the L_1 side of the Moon, as observed in Figures 3b and 3d, a large loop on the L_2 side, in Figure 3c, and departures with a 'sharp turn', in Figure 3e.
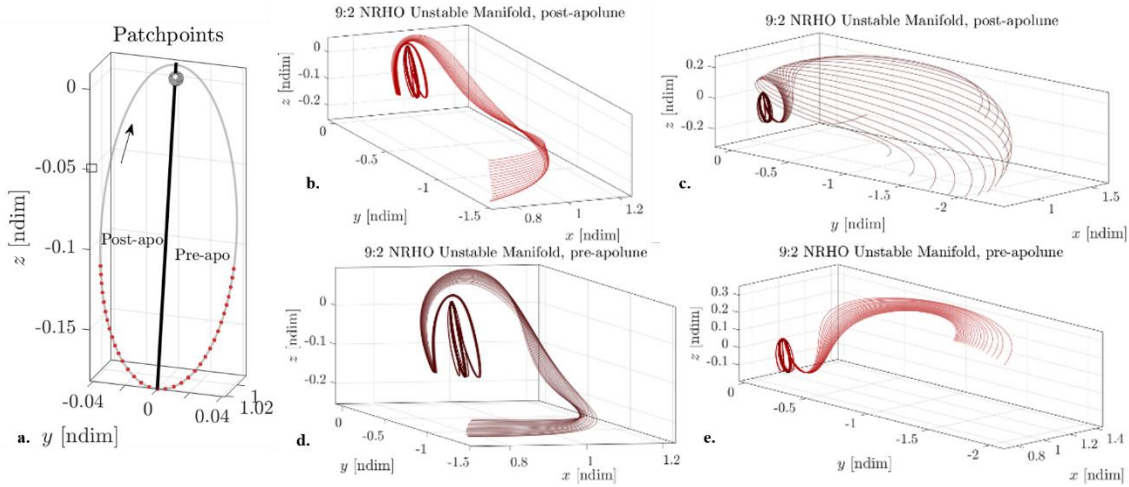

Figure 3. Manifold structures near apolune of the 9:2 NRHO in the CR3BP

These stability results are extended to the Earth-Moon-Sun Bicircular Restricted 4-Body Problem (BCR4BP). Previous work[8] demonstrated that specific NRHOs corresponding to a synodic resonance, including the 4:1 and the 9:2 NRHOs, are transitioned to the BCR4BP while maintaining the geometry, the perilune and apolune radii and the linear stability properties. The 4:1 NRHO in the CR3BP and its BCR4BP counterpart appear in Figure 4a. The six-dimensional angle between the stable and unstable eigenvectors along the 4:1 NRHO in each model is plotted in Figure 4b. Note that the angle is computed for four revolutions of the 4:1 NRHO in the CR3BP, accommodating the longer period of the 4:1 NRHO in the BCR4BP. Consistent with the angle between unstable and stable eigenvectors of the 9:2 NRHO in Figure 2, the angle for the 4:1 NRHO is less than 10 degrees near perilune for both the CR3BP and the BCR4BP 4:1 NRHOs. Similarly, the eigenvectors are oriented in distinctly different directions closer to apolune, as observed for each revolution of the 4:1 NRHO in the BCR4BP in Figure 4b. The 4:1 NRHO in the BCR4BP includes four lobes: two on the L_1 side of the CR3BP 4:1 NRHO and two on the L_2 side of the CR3BP 4:1 NRHO. For the lobes on the L_1 side, the angle between stable and unstable eigenvector directions exceeds 100° near apolune. On the L_2 side, the angle is approximately 70° near apolune. For reference, the angle along the 4:1 NRHO in the CR3BP is approximately 80° close to apolune. The stability characteristics and the eigenvectors direction in the 4:1 synodic resonant NRHO remain consistent when transitioned to the BCR4BP.
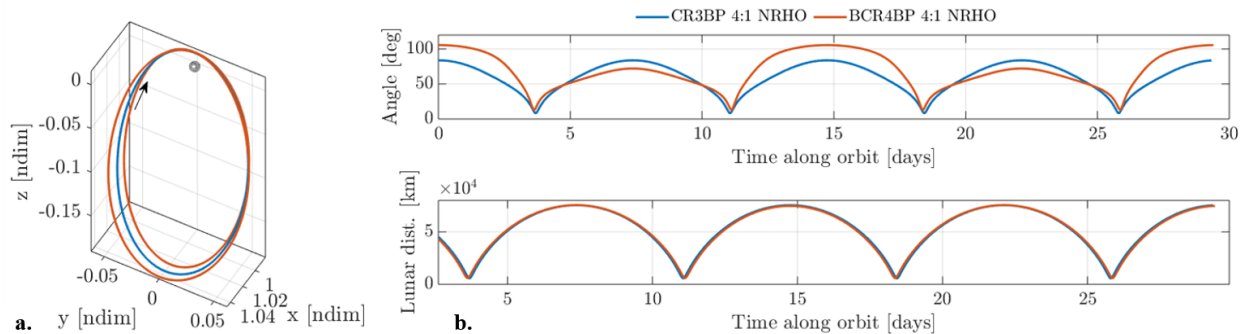
Figure 4. CR3BP 4:1 NRHO in blue and BCR4BP 4:1 NRHO in orange, as viewed in the Earth-Moon rotating frame (a). Angles between unstable and stable eigenvectors of each NRHO (b).

The BCR4BP 4:1 NRHO is discretized and a set of patch points close to the apolune is selected, as apparent in Figure 5. A representative subset of the manifolds is constructed and plotted in purple in Figure 5. The departing flow near apolune is structured and consistent with Figure 3e and the departure trajectories previously computed.[2,3] Manifold structures are well defined near apolune of the 4:1 NRHO in the CR3BP and the BCR4BP. Near perilune, the angle between stable and unstable eigenvector directions is less than 10°. Thus, accurate computation of the manifolds in the lunar vicinity is challenging.
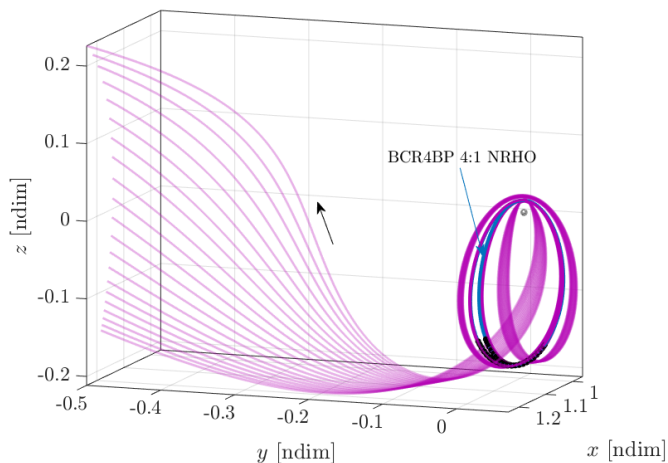

Figure 5. Representative unstable mainfolds near apolune in the BCR4BP 4:1 NRHO.

ESCAPE TO HELIOCENTRIC SPACE

Once an object has departed the NRHO, its destination depends on the effects of the Sun, the Earth, and the Moon on the trajectory. The object may impact the Moon, it may remain in orbit in the Earth-Moon vicinity, or it may escape to heliocentric space. Various objects departing the Gateway may be delivered to heliocentric space for disposal or for science and exploration applications. Examples include spent logistics modules or disposable ascent modules, debris or wet trash, and cubesats. For any object attempting to depart the Earth-Moon vicinity with a relatively small maneuver, two basic prerequisites are necessary. First, the energy in the Sun-B_1 frame must be sufficient for the time-varying ZVSs to be open at the E_1 and E_2 libration points in the Sun-B_1 system. Second, the orientation within the Sun-B_1 frame must be favorable for the solar gravity to pull the object through the portals. The current investigation considers each of these constraints for specific examples, employing maps and other visuals to condense the large data space.

Energy in the Sun-B_1 system: Hamiltonian behavior

The Hamiltonian in the Sun-B_1 system is a representation of the energy of a given trajectory; as defined here, a lower value of the Hamiltonian represents a higher energy. As discussed, the time-varying Hamiltonian describes osculating ZVSs that govern the allowable motion of an object in the Sun-Earth-Moon BCR4BP. To achieve escape from the Earth-Moon vicinity, the energy must be sufficiently high, or the Hamiltonian must be appropriately low, such that the ZVSs allow open portals at the E_1 and E_2 libration points in the Sun-B_1 system. For example, a sample escaping trajectory appears in the Earth-Moon rotating frame in Figure 6a and in the Sun-B_1 rotating frame in Figure 6b in the ephemeris model. The Sun-B_1 Hamiltonian appears as a function of time in Figure 6c; the values of H corresponding to the E_1 and E_2 portals are indistinguishable at this scale and appear as a black line. The MI over time is plotted in Figure 6d. In each image, the trajectory is colored orange while the orbit is maintained prior to the separation maneuver. Note the large oscillations in the Sun-Earth Hamiltonian as the spacecraft remains under the close influence of

lunar gravity, and the near-periodicity in the MI prior to the separation burn. At time t = 0, a separation burn is executed, and the trajectory is colored pink while it remains near the NRHO. The MI slowly starts to diverge from its periodic behavior. After about 38 days, the value of the MI exceeds 0.1, and the trajectory, now colored blue in Figure 6, is considered departed from the NRHO. The Hamiltonian at this point is below the value corresponding to the E_1 and E_2 libration points, and the spacecraft is sufficiently energetic to escape the Earth-Moon vicinity. Approximately 60 days after the separation burn, the spacecraft passes through the E_1 portal, and the trajectory, now in green, is considered to be in heliocentric space.
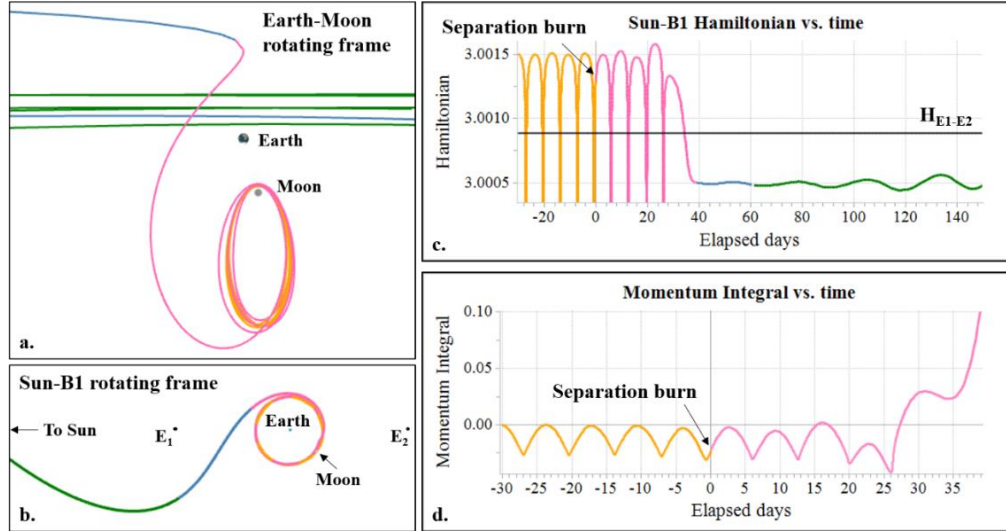

Figure 6. Escaping trajectory in the Earth-Moon rotating frame (a), the Sun-B_1 rotating frame (b) and the corresponding Sun-B_1 Hamiltonian (c) and Momentum Integral (d).

The departing trajectory in Figure 6 represents a single successful heliocentric departure trajectory. Further examination of the Hamiltonian in the ephemeris force model yields insight into the relationship between maneuver magnitude and the resulting energy in the Sun-B_1 system. Specifically, for separation at a given location along the NRHO, maneuvers are explored that result in Hamiltonian values sufficiently low to correspond to E_1 and E_2 portals that are open, allowing escape to heliocentric space. A maneuver with location, direction and magnitude leading to consistent and predicable behavior is sought. Consider a separation maneuver applied in the inertial velocity direction at every perilune for 56 consecutive revolutions within the NRHO, or for approximately one year. A given maneuver can lead to:
1. Consistent behavior across the year with energy insufficient to allow escape from the vicinity of the Earth through the Sun-B_1 portals.
2. Inconsistent behavior throughout the year, with some departing trajectories possessing sufficient energy to escape and others with insufficient energy to escape
3. Consistent Hamiltonian values reflecting sufficient energy to escape from the vicinity of the Earth for a maneuver at every perilune passage throughout the year.

For reliable heliocentric escape, the third option is desirable. However, a larger maneuver does not necessarily correspond to a higher energy or a more reliable result. For example, the Hamiltonian as a function of time appears in Figure 7a-c for three small values of Δv magnitude delivering separation burns in the inertial velocity direction at perilune. In Figure 7a, a maneuver magnitude of 0.1 m/s leads to departure from the NRHO after eight additional revolutions within the NRHO, with values of the Hamiltonian consistently higher than the value at the E_1/E_2 portals (represented by the black line). A lunar flyby after about 100 days shifts the Hamiltonian value significantly in some cases. In the Figure 7b, a higher separation maneuver of 0.7 m/s results in inconsistent departure times from the NRHO and corresponding inconsistent Hamiltonian behavior from one revolution to the next. In Figure 7c, a maneuver of 1 m/s yields departure after 4 additional revolutions in the NRHO. After departure from the NRHO, the Hamiltonian is below the black line in nearly all cases, indicating sufficient energy to escape the Earth-Moon vicinity. When the orientation of each departing trajectory is appropriately aligned in the Sun-B_1 frame, it is able to escape. Thus, a maneuver magnitude of 1 m/s yields favorable behavior when the separation burn is performed in the

inertial velocity direction at perilune for most revolutions. However, a small variation in magnitude breaks the consistent patterns of behavior: a variation larger than +/- 0.1 m/s leads to inconsistent or unfavorable behavior. Thus, errors in navigation or maneuver execution render a 1 m/s maneuver magnitude unreliable for heliocentric escape.
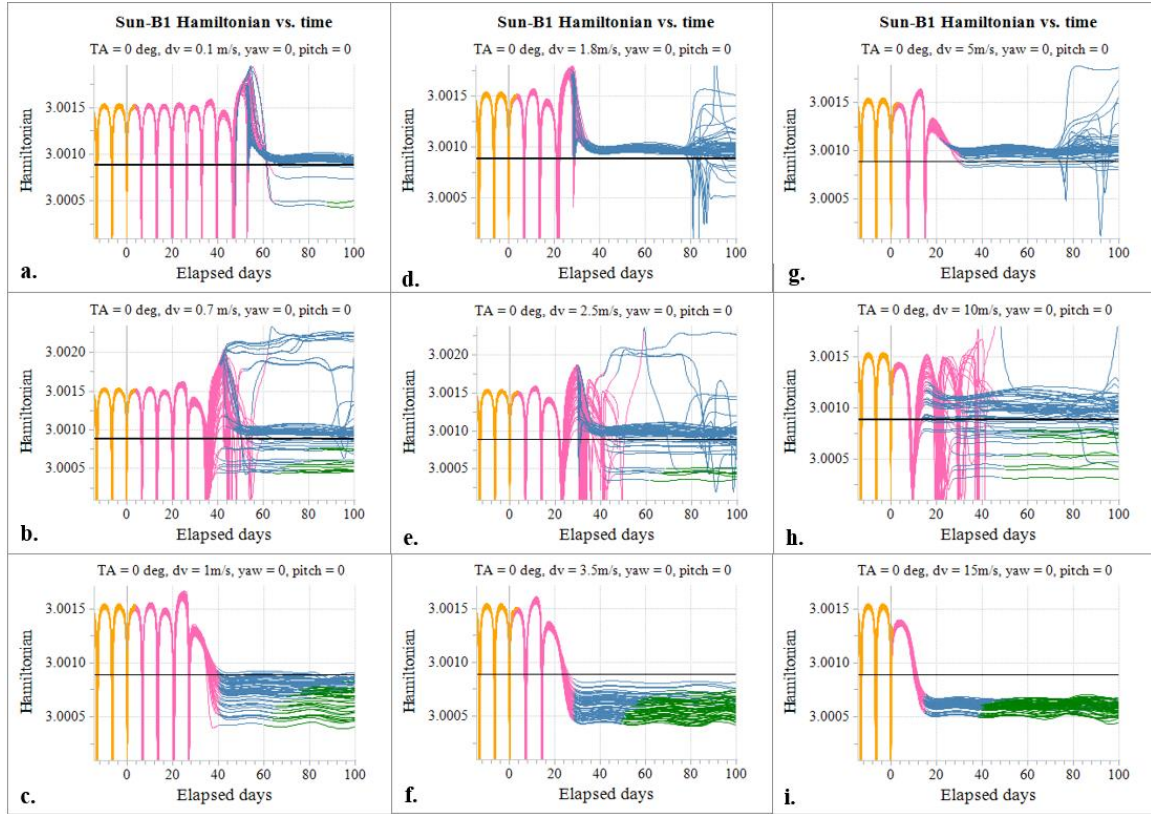

Figure 7. Hamiltonian as a function of time for low (left), medium (center), and high (right) maneuver magnitudes for 56 consecutive revolutions in the NRHO

The same pattern is repeated as the maneuver magnitudes increase, with Hamiltonian values consistently too large to allow escape, followed by inconsistent escape behavior as the trajectory transitions from departure after N revs in the NRHO to departure in N-M revs, followed by consistently low Hamiltonian values as the maneuver magnitude increases. Then, the Hamiltonian increases along with maneuver magnitude until inconsistent behavior is again observed. In Figures 7d to 7f, maneuvers of 1.8, 2.5, and 3.5 m/s yield earthbound, variable, and energetic NRHO departures, respectively. Similarly, in Figures 7g to 7i, separations burns of 5.5 m/s, 10 m/s, and 14 m/s display low energy, inconsistent, and high energy departures, respectively, as the departure transitions from 2 additional revolutions within the NRHO to immediate departure after the separation burn.

A low separation burn magnitude of 1 m/s, a medium Δ𝑣 magnitude of 3.5 m/s, and a larger maneuver magnitude of 15 m/s all yield consistent high-energy departures. Note that the window of reliable high energy departures around the nominal value increases along with the maneuver magnitudes. A tolerance of only +/- 0.1 m/s is available to ensure high energy departure in the 1 m/s case, while a variation of +/- 0.4 m/s continues to produce consistently low Hamiltonian values for 3.5 m/s separation burns. If the nominal maneuver is 15 m/s, a variation of +/- 2 m/s continues to yield Hamiltonian values that allow escape from the Earth-Moon vicinity. The higher magnitude is more robust in response to errors but does not remove the importance of Sun orientation or maneuver location and direction.

The Hamiltonian plots in Figure 7 represent separation from a single location along the NRHO (perilune) and in a single maneuver direction (inertial velocity direction). While separation at perilune is effective for achieving escape, both the Gateway and the departing object are susceptible to perturbations and errors in the sensitive region near perilune; separation at other locations along the NRHO may be more attractive. To

seek other potential separation locations, a set of Hamiltonian maps is developed to explore the maneuver design space for a variety of burn locations, directions, and magnitudes and to identify separation maneuvers that yield robust, high-energy departures. A sample appears in Figure 8a for 1 m/s separation burns departing from perilune at a particular revolution along the 9:2 NRHO and in every possible direction. Each separation location is parameterized by osculating true anomaly, TA, although the NRHO is not a Keplerian orbit. The osculating TA along the 9:2 NRHO is depicted in the rotating frame in a concurrent study.[11] The center of the map represents a maneuver in the inertial velocity direction. The horizontal axis represents maneuver yaw direction with respect to the velocity vector and ranges from -180° to 180°. The maneuver pitch angle is plotted along the vertical axis and spans -90° to 90°. The velocity, normal, and binormal directions are marked on the map as white points. Each colored point on the map represents the outcome of a separation burn. If the Hamiltonian at NRHO departure, defined as the time when the momentum integral reaches a value of 0.1, is greater than H_{E1-E2}, then the energy is insufficient to escape, and the point is colored blue. If the Hamiltonian at NRHO departure represents sufficient energy to escape, that is, $H < H_{E1-E2}$, the point is colored red. If the spacecraft impacts the Moon prior to NRHO departure, the point is colored yellow; the lunar impact cases are explored in detail in a following section. There are several observations to note. First, the Hamiltonian maps do not necessarily reveal a maneuver that leads to heliocentric escape, only whether the energy at departure is sufficient to escape. Second, the maps in Figure 8 are generated in the ephemeris force model, so the results for a given NRHO location may vary from one revolution to the next. However, the maps yield useful information on favorable locations and directions for maneuvers that yield trajectories with sufficient energy for heliocentric escape. They also provide insight concerning the robustness of a maneuver in the presence of navigation and maneuver execution errors as well as reliability from one revolution to the next.
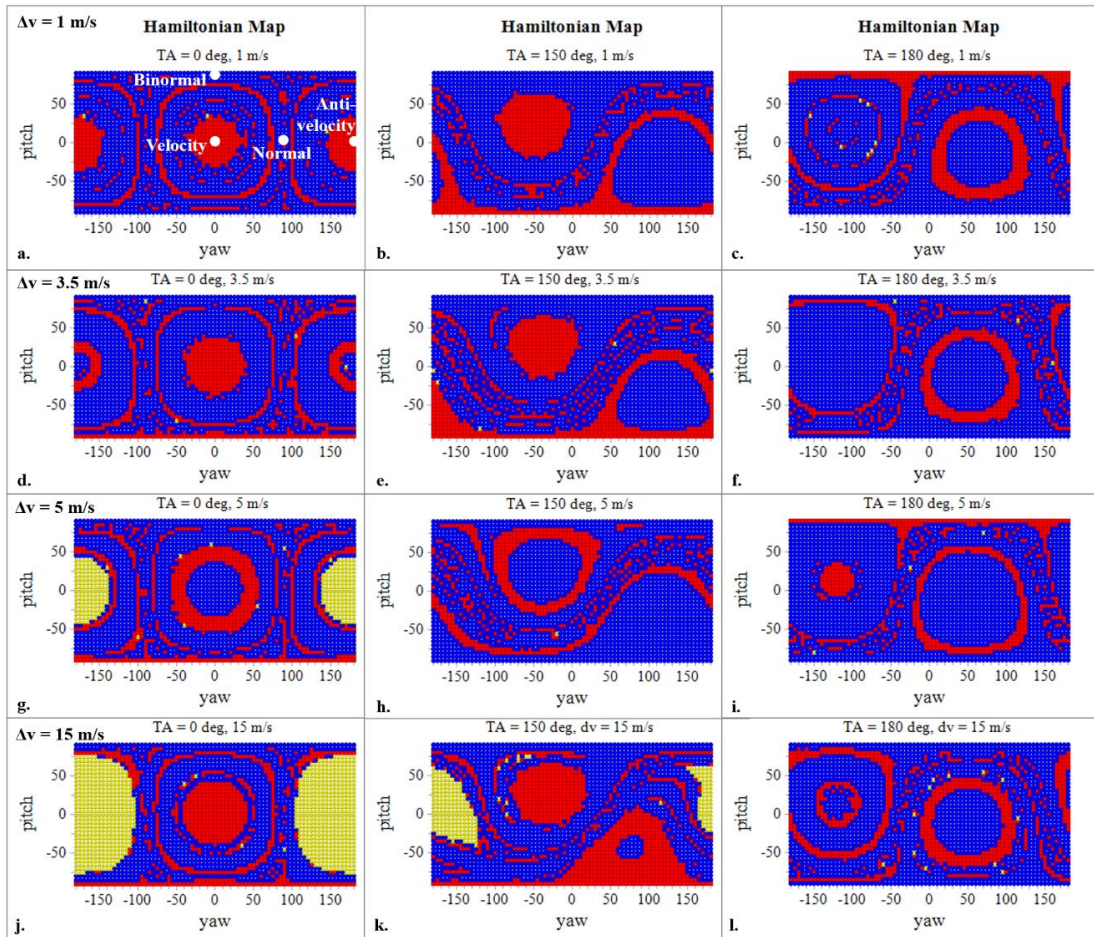

Figure 8. Hamiltonian maps representing separation burns in three locations along the 9:2 NRHO.

Recall the 1 m/s separation burn executed at perilune in the inertial velocity direction depicted in Figure 7c. This maneuver results in a Hamiltonian value, *H,* at departure that is low enough to allow heliocentric escape along most revolutions; the maneuver is represented by the point directly in the center of Figure 8a, which is correspondingly colored red. It is surrounded by a region of other red points, implying that the departure is robust to a pointing error in the separation maneuver within the yaw and pitch boundaries of the red region. As the maneuver direction changes further, the red region is surrounded by blue areas representing departures insufficiently energetic to escape, and then by thin red rings representing directions that lead to high energy departures but without tolerance for pointing errors. A second large red region exists in the anti-velocity direction in Figure 8a. As the departure location varies, the red regions shift from the velocity and anti-velocity directions to areas on the map representing other burn directions, or they change from solid regions to rings. For example, a map representing departure from a true anomaly TA = 150° appears in Figure 8b, as this location is notably favorable from a Hamiltonian perspective. Note the solid red region centered at yaw = -50° and pitch = 50°, representing a candidate for a separation burn away from perilune. A departure location further along the NRHO at apolune, or TA = 180°, appears in Figure 8c. In this map, the solid red region is replaced by red rings, representing departures that are less robust to navigation and pointing errors. As the burn magnitude changes, the characteristics of the maps also evolve. Though not depicted in the figure, the red region centered on the velocity direction disappears as the magnitude passes 1.1 m/s, signifying a narrow tolerance to errors in burn magnitude. Large red regions return to the maps for separation burns of 3.5 m/s; corresponding maps appear for the same three locations along the NRHO in Figures 8d to 8f. As the Δ*v* magnitude is further increased to 5 m/s, velocity-direction maneuvers at perilune are insufficiently energetic to escape and are represented by the blue region in the center of the map in Figure 8g. The corresponding time history of the Hamiltonian for a 5 m/s separation from perilune in the velocity direction at perilune appears in Figure 7d, demonstrating consistently insufficient departure energies. Maneuvers in the anti-velocity direction with a 5 m/s burn at perilune lead to lunar impact, as is apparent from the large yellow region on the map, and thus are not candidates for heliocentric escape. As departure moves along the NRHO, as in Figures 8h and 8i, rings of sufficient energy remain visible but large solid regions do not appear in the maps for 5 m/s separation burns. Increasing the energy further to 15 m/s, however, yields large, robust red regions in the Hamiltonian maps at both perilune and at TA = 150°. Note the large yellow region surrounding the anti-velocity direction; these points correspond to lunar impact trajectories, which are examined in detail in the CR3BP in the next section. Though not included in the current study, maps are generated for the 4:1 NRHO as well, identifying maneuver parameters that lead to energetic departure and explaining why 1 m/s burns in the velocity direction at perilune along the 4:1 NRHO do not lead to heliocentric departure.

The maps in Figure 8 represent departure along a single revolution in the quasi-periodic reference 9:2 NRHO. Overlaying maps representing sequential revolutions within the NRHO reveals the robustness of a given separation burn to variations in the NRHO. For example, consider the maps in Figure 9. Each map represents departure at a particular burn magnitude and from a particular separation location. In this case, the red points reflect separation burns that yield sufficient energy at departure for heliocentric escape for each of 9 consecutive revolutions (representing 2 synodic periods in the NRHO and, thus, each possible Sun-Earth-Moon-Spacecraft geometry). The blue regions represent maneuvers that lead to insufficient departure energy for at least one revolution among the nine. Darker blue regions signify burns resulting in sufficient energy for escape from the first revolution tested but insufficient energy in later revolutions. Similarly, bright yellow regions represent burns that always result in lunar impact, while darker yellow areas denote maneuvers that lead lunar impact during at least one but not all of the nine revolutions. For a 1 m/s burn from perilune, in Figure 9a, while a red ring remains in the map, the velocity direction itself is not consistently robust from revolution to revolution; separation from perilune along some revolutions within the NRHO yields lower-energy departures. At TA = 150°, no burn direction consistently leads to sufficiently energetic departure. Therefore, while a 1 m/s maneuver direction is available that yields energetic departure along any given revolution, no single direction is reliable over every revolution of the nine tested. If the burn magnitude is increased to 3.5 m/s, however, a velocity-direction maneuver at perilune and a small region near yaw = -25° and pitch = 50° at TA = 150° yield consistent high-energy departures across all nine revolutions. Similarly, with a burn magnitude of 15 m/s, dependable departure directions exist at both perilune and at TA = 150°.

In Figures 8 and 9, maps corresponding to three possible separation burn locations are depicted. To explore the continuum of burn locations along the NRHO, similar maps are stacked into a 3D figure, with

yaw and pitch represented along the two horizontal axes and maneuver TA along the vertical axis. Examples appear in Figure 10 for burn magnitudes of 3.5 m/s and 15 m/s. In these maps, only the points corresponding to departures with sufficient energy to escape are included, each colored according to its Hamiltonian value at departure. Maneuvers that result in insufficiently energetic departures or lunar impacts are excluded. In both cases, a sphere at the center of the map signifies a group of robust successful maneuvers centered on the velocity direction at perilune. In Figure 10a, for a 3.5 m/s separation burn, the sphere extends from -60° < TA < 60° in location, and from -30° < yaw < 30° and -30° < pitch < 30° in direction. As the burn moves away from perilune, another region associated with successful separation burns appears near TA = 150°, marked in Figure 10a by an arrow. A similar map appears in Figure 10b for Δv = 15 m/s. At the higher burn magnitude, two regions representing burns that result in energetic departures exist away from perilune; one near TA = 150° and another near TA = -150°; both are marked by arrows. Outside of these regions, only narrower rings of energetic departures exist; hence the focus on TA = 0° and TA = 150° in this study.
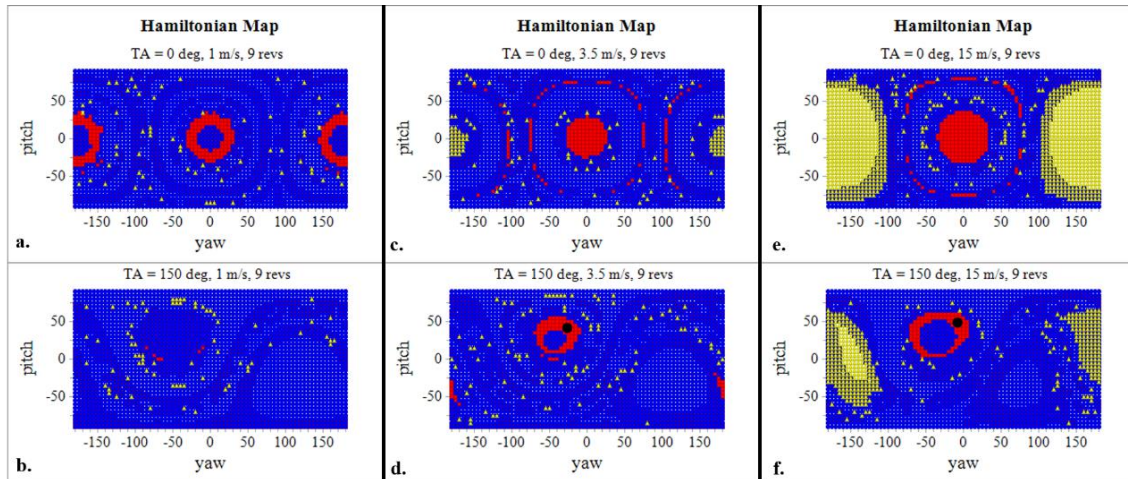

Figure 9. Hamiltonian maps for departure from 9 consecutive revolutions along the 9:2 NRHO
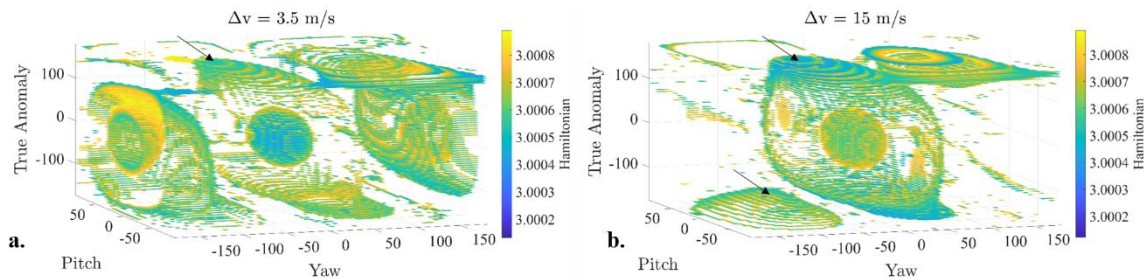

Figure 10. 3D Hamiltonian maps for two separation burn magnitudes

The robustness of the departure energy for selected separation burns in the presence of navigation and maneuver execution errors are tested via Monte Carlo analysis. Because orbit determination errors are expected to be higher at perilune than elsewhere in the orbit,[12] the analysis assumes 3σ navigation errors of 10 km in position and 10 cm/s in velocity for departures at perilune and errors of 1 km in position and 1 cm/s in velocity for departures at TA = 150°; the other errors included in the analysis are described previously.

The first set of Monte Carlo results addresses robustness along a single revolution within the reference NRHO. That is, for a given departure epoch, the reliability of a separation burn is explored. In each case, 100 Monte Carlo trials are executed and the number of trials that lead to heliocentric escape after a 200-day propagation is recorded. The results appear in Table 2. The first set of results corresponds to departures at perilune, as in the left-hand column in Figure 8. Departures in the velocity direction (yaw = pitch = 0°) lie in the center of the large red regions in Figures 8a, 8d, and 8j. For a 1 m/s maneuver, the navigation errors perturb the departures significantly, and only 33 of the 100 trials achieve escape to heliocentric space. Increasing the Δv magnitude to 3.5 m/s improves the robustness, with 89% of trials successfully escaping the Earth's vicinity. For departures from perilune, a burn of 15 m/s results in 100% success; the larger burn

magnitude is necessary to ensure escape to heliocentric space in the presence of the larger navigation errors expected near perilune. Maneuvers with a non-zero pitch angle are also explored. Such options exist as narrower bands in the Hamiltonian maps in Figure 8. The results from one sample direction (yaw = 0°, pitch = 75°) for 1 m/s and 3.5 m/s Δv magnitudes appear in Table 2, without improvements in robustness. However, by moving away from perilune, the expected navigation errors decrease, and reliability improves. Consider departures from the Gateway at TA = 150°, as in the center column in Figure 8. For maneuver magnitudes equal to 1 m/s, 3.5 m/s, and 15 m/s, large red regions exist in the maps corresponding to sufficiently energetic departures. These regions are characterized by negative yaw and positive pitch values. A 1 m/s separation maneuver directed in the center of the corresponding red lobe such that yaw = -50° and pitch = 25° results in a 97% success rate. Increasing the Δv magnitude to 3.5 m/s and aligning the direction with yaw = -25° and pitch = 25° yields all 100 trials escaping from the Earth-Moon vicinity. Similarly, a 15 m/s burn results in 100% of the trials achieving heliocentric escape. Narrower bands of red also exist in the Hamiltonian maps for these three maneuver magnitudes for departures at TA = 150°. For example, separation burns of 1 m/s and 3.5 m/s in a direction defined by yaw = 50° and pitch = -25° yield 91% and 77% success respectively. A maneuver of 15 m/s directed such that yaw = 120° and pitch = -60° leads to 100% heliocentric escape. As expected, selecting a burn direction centered in one of the larger red regions leads to improved reliability.

Table 2. Monte Carlo trials for separation burns over a single NRHO revolution: successful escapes

	TA = 0 (perilune, 10 km/10 cm/s nav errors)		TA = 150 (away from perilune, 1 km/1 cm/s nav errors)			
	yaw = 0, pitch = 0	yaw = 0, pitch = 75	yaw = -50, pitch = 25	yaw = -25, pitch = 25	yaw = 50, pitch = -25	yaw = 120, pitch = -60
1 m/s	33/100	43/100	97/100		91/100	
3.5 m/s	89/100	38/100		100/100	77/100	
15 m/s	100/100			100/100		100/100

The results in Table 2 represent departures along a single revolution in the NRHO. Recall from Figure 9 that maneuver directions leading to escape vary from one revolution to the next in the ephemeris force model. To explore robustness across many revolutions within the reference NRHO, an expanded Monte Carlo analysis is run. The analysis focuses on the most reliable maneuvers identified in Table 2, that is, separation burn magnitudes of 3.5 m/s and 15 m/s, and separation locations at TA = 150°. For a given separation burn magnitude, direction, and true anomaly, 10 trials are run for departures at TA = 150° along each of 56 consecutive revolutions within the reference NRHO, for a total of 560 trials over a one-year span. The maneuver directions are selected from the maps in Figure 8d and 8f, marked with black dots. The maps suggest that the selected maneuver directions may yield sufficient energy to escape across all revolutions. In fact, the maps' predictions hold over the Monte Carlo analysis. In each case, though not all trajectories achieve heliocentric escape, 100% of the Monte Carlo trials depart the NRHO with energy sufficient to allow escape. For a 3.5 m/s burn at TA = 150° directed such that yaw = -25° and pitch = 35°, 396/560 trials escape to heliocentric space. For a 15 m/s separation burn in the yaw = -5°, pitch = 40° direction, 460/560 trajectories escape. Again, every departing trajectory is sufficiently energetic to escape, though escape does not always occur. The departing trajectories that fail to achieve heliocentric escape remain earthbound because of their unfavorable orientation in the Sun-B_1 frame. It is also important to consider the safety of the Gateway spacecraft as objects depart. The risk of recontact with the Gateway is explored in depth in a previous study,[4] and a concurrent study explores the risk of recontact during the specific successful heliocentric escapes in the current Monte Carlo example.[11] All four of the maneuvers investigated in this section depart the NRHO without a risk of recontact with the Gateway.

In summary, for any revolution along the NRHO, maneuver locations, magnitudes, and directions can be identified that yield energy sufficient for escape from the Earth-Moon vicinity. Hamiltonian maps characterize the maneuver design space and allow selection of maneuver magnitudes and directions that yield sufficiently energetic departures from the NRHO. Separation locations away from perilune are associated with smaller navigation errors and, thus, are associated with more robust departure energies for small separation burns. In a Monte Carlo analysis, 100% robustness is observed for maneuver magnitudes as low as 3.5 m/s for maneuvers away from perilune, while 15 m/s is required for reliable departures from perilune. A 1 m/s burn does not provide 100% robust departure energy in the presence of navigation errors, even away from perilune, especially if a consistent maneuver location and direction is desired from one revolution to the next. In all cases, successful heliocentric escape also requires appropriate Sun-B_1 orientation.
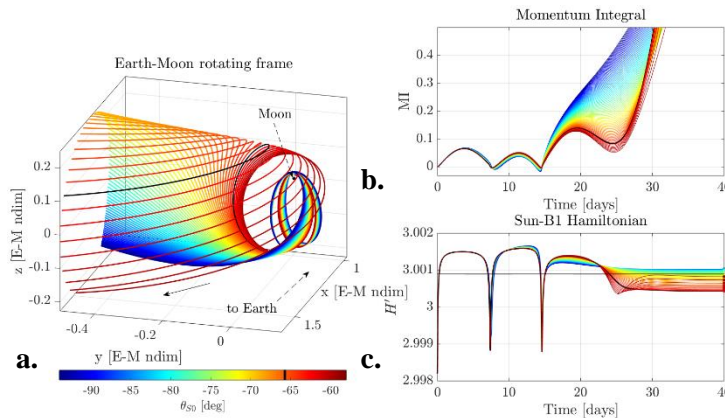
NRHO Departure geometry and Sun-B_1 Hamiltonian

The relationship between departure geometry from the 9:2 NRHO and the Sun-B_1 Hamiltonian value is explored in the BCR4BP. For a fixed magnitude and direction maneuver at perilune along the NRHO, the initial position of the Sun is varied, and the state is propagated using the BCR4BP equations of motion. The resulting trajectories for a maneuver of 5 m/s in the velocity direction are plotted as viewed in the Earth-Moon rotating frame in Figure 11. The trajectories are propagated for
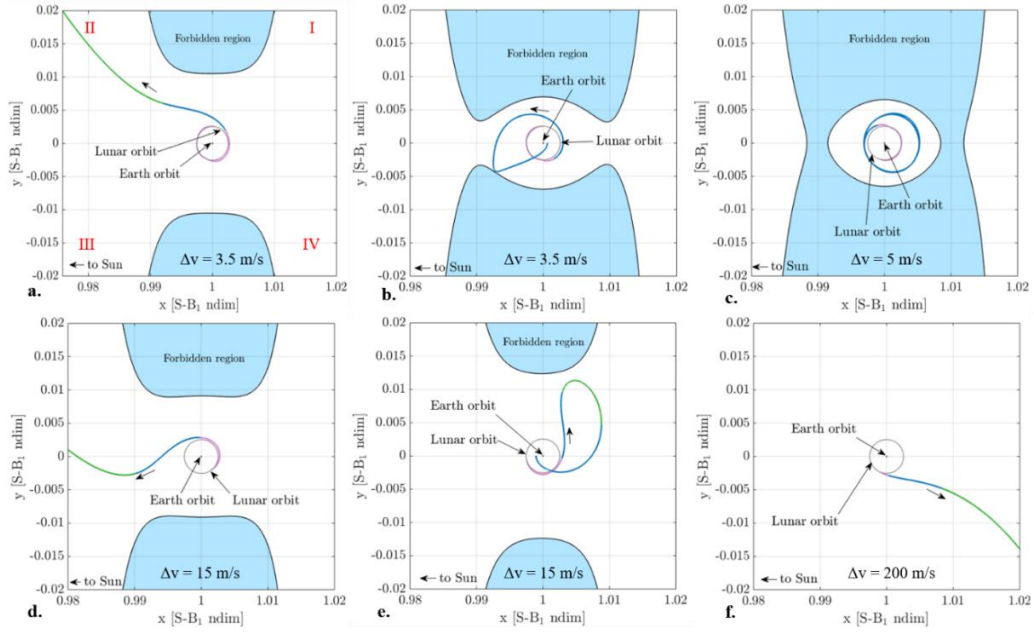
Figure 11. Departure geometries from the 9:2 NRHO in the BCR4BP for a 5 m/s maneuver (a). Associated momentum integral (b) and Sun-B_1 Hamiltonian (b)

an arbitrary duration of 40 days, a sufficient time for all trajectories to reach a plateau in Sun-B_1 Hamiltonian value, plotted in Figure 11c. Multiple geometries are observed in Figure 11a. Trajectories plotted in shades of blue, corresponding to an initial Sun angle between -100° and -80°, depart the NRHO near apolune and possess a negative *z*-coordinate after departure. These types of geometries do not offer sufficient energy to escape the Earth-Moon system. As the initial Sun angle increases, the departing trajectories stretch toward the Moon, and the resulting Sun-B_1 Hamiltonian values decrease. The trajectory possessing the lowest Sun-B_1 Hamiltonian after departure from the NRHO, that is, the most energetic trajectory, is plotted in black in Figures 11a to 11c. Its geometry is consistent with previously observed successful disposal trajectories: a sharp 'turn' after departure from the vicinity of the Moon. As the initial Sun angle further increases, for lines colored in shades of red in Figure 11, another loop begins to form around the Moon and the Sun-B_1 Hamiltonian values start to increase. This new loop indicates a transition in the solution geometry, from 2 revolutions to 3 revolutions before departure. The departure metric, i.e., the momentum integral, is plotted in Figure 11b, and exhibits signs of the shift in geometry as well: trajectories with an extra loop with respect to the Moon also possess an additional crest in their associated momentum integral value. Departure geometry from the lunar vicinity and the evolution of the Sun-B_1 Hamiltonian value are closely related; by appropriately selecting the NRHO departure geometry, favorable energy in the Sun-B_1 frame is achieved.

Orientation in the Sun-B_1 System: Maneuver timing

After a separation maneuver is selected that yields sufficient energy at NRHO departure, a second prerequisite must be met to ensure escape to heliocentric space. Once the spacecraft has departed the NRHO, solar gravity significantly affects the trajectory. The orientation of the orbit in the Sun-B_1 frame determines whether the impact of solar gravity circularizes the orbit around the Earth-Moon barycenter, preventing escape, or elongates the orbit, facilitating escape to heliocentric space.[13] A previous analysis[3] details departures from the NRHO in quadrant I or quadrant III in the Sun-B_1 rotating frame with the appropriate energy and eccentricity that lead to heliocentric escape, where the B_1-centered quadrants are defined in red text in Figure 12a. The higher the energy at departure, the less precise the required orientation to allow escape through the E_1 and E_2 portals in the ZVSs. For example, consider the trajectories in Figure 12. In each image, the ZVS is defined by the Sun-B_1 Hamiltonian value along the trajectory after departure from the NRHO, and the spacecraft cannot cross into the forbidden region, shaded in blue. In Figure 12a, the Hamiltonian value is sufficiently low and the trajectory is oriented appropriately for the 3.5 m/s separation burn to lead to escape. In contrast, in Figure 12b, while the ZVSs are open, the orientation is not favorable and the trajectory does not escape. Figure 12c represents a 5 m/s separation maneuver that results in insufficient energy; the ZVSs are closed at both E_1 and E_2. Figures 12d and 12e each represent a 15 m/s separation burn; though the Hamiltonian is lower in Figure 12e and the portal is open further, the orientation is unfavorable and the trajectory remains earthbound. To ignore orientation entirely, a separation burn as high as 200 m/s is required, as in Figure 12f. In this case, the ZVSs are entirely out of plane and any orientation likely leads to escape. Since a Δ*v* of such a high magnitude is operationally infeasible, smaller burns must be executed such that the departing trajectory is elongated by the Sun's gravity and pulled through the E_1 or E_2 portal.

Figure 12. Escaping and earthbound trajectories near the Moon and ZVSs defining forbidden regions in the BCR4BP.

The orientation of the escaping path in the Sun-B_1 rotating frame depends on (1) the time between the separation maneuver and the MI value indicating departure from the NRHO and (2) the orientation of the maneuver itself. Thus, for a given set of burn parameters, the location of the burn in the Sun-B_1 frame is mapped to the outcome. Three candidate separation burns from Table 2 are again investigated. This time, the burn locations are plotted in Figure 13 in the Sun-B_1 rotating frame, colored according to their fate. Maneuvers that lead to heliocentric escape are colored red, while burns that result in earthbound trajectories appear in blue. Recall that the Hamiltonian values at NRHO departure for each of the 560 trajectories represented in the maps in Figure 13 are sufficiently low to allow heliocentric escape; however, only the burns marked in red result in a trajectory oriented appropriately to allow solar gravity to facilitate escape from the Earth-Moon vicinity. Note that nine clusters of maneuvers appear in each plot; these nine burn locations repeat because of the 9:2 resonance of the NRHO with the lunar synodic period. In each case, five or six of the nine possible maneuver orientations result in consistent heliocentric escape over the one-year analysis. All of the earthbound trajectories originate from maneuvers in the remaining orientations, with the 15 m/s burns resulting in fewer total earthbound outcomes. The specific maneuver locations that lead to successful escapes depend on the burn parameters. For example, in Figure 13a, burn locations along the *x* axis in the Sun-B_1 rotating frame for a 3.5 m/s burn at TA = 150° result in successful escapes; the same is not true in Figure 13c: burns of 15 m/s from perilune near the Sun-B_1 rotating *x* axis lead to earthbound orbits. The maneuver maps in Figure 13 show, over time, the correlation between burn location and departure orientation, and, thus, successful heliocentric escape. A map is specific to each set of burn parameters.
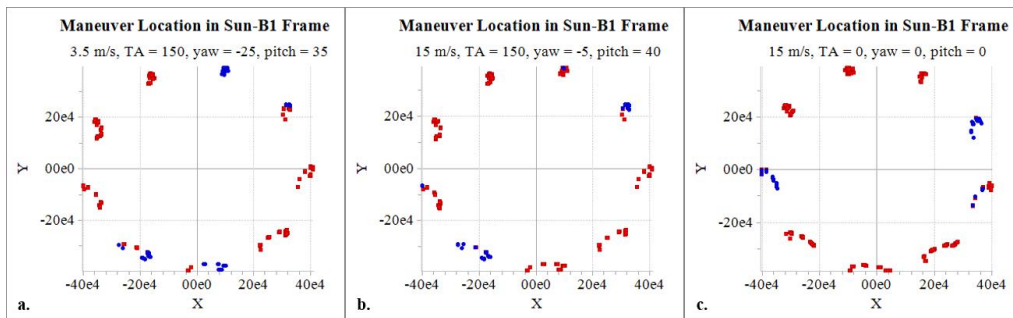

Figure 13. Maneuver orientations in the Sun-B_1 frame in the ephemeris model.

14

LUNAR IMPACT TRAJECTORIES

For some Gateway applications, it may be desirable to impact the lunar surface after departure from the NRHO. Lunar impact trajectories are of interest to lunar science missions, ejecta studies, and potential disposal of objects not intended for heliocentric space.[14] Understanding the behavior of lunar impact trajectories originating from the NRHO also characterizes risk and may drive constraint definition for mission designs in which lunar impact is not desired and aid in avoidance of lunar heritage sites. As with escaping trajectories, the qualitative and quantitative nature of lunar impact trajectories from the NRHO are highly dependent on the location, magnitude and direction of the departing maneuver. Lunar impact trajectory characteristics of interest include the location in pitch-yaw space of the separation maneuvers that lead to impact, the velocity, angle, and location of lunar impact on the surface, and the time to impact. Time to impact provides a quantifiable metric for impact geometry. Analysis of the lunar impact trajectories is performed in the CR3BP to eliminate epoch dependence and to leverage the Jacobi constant. The current analysis is limited to orbits that remain in the lunar vicinity.

Theoretical Bounding of Impact Speed

The speed relative to the lunar surface at impact is important for various applications, including kinetic impactors and ejecta analysis. The CR3BP supplies a theoretical bound on the extrema for impact speeds resulting from maneuvers in the 9:2 NRHO. The Jacobi constant in Equation (1) is a first order integral of the motion in the CR3BP and remains constant across any continuous ballistic trajectory. Assuming a given initial Jacobi constant value, Equations (1) and (2) are rearranged to yield the relative velocity magnitude at any point along the trajectory as a function of position and J, i.e.

$$v = \sqrt{(x^2 + y^2) + \frac{2(1-\mu)}{d} + \frac{2\mu}{r} - J}. \qquad (5)$$

The impact condition bounds $d, r,$ and $(x^2 + y^2)$. The distance to the Earth at impact, d, is never greater than that of the lunar orbital radius plus the lunar radius; the distance to the Moon at impact, r, is always equal to the lunar radius, and the quantity $(x^2 + y^2)$ is bound by the square of the bounds on d. Thus, the minimum and maximum speeds at impact are evaluated for a given initial Jacobi constant value and a given maneuver magnitude at perilune in both the anti-velocity and velocity directions, respectively. Note that the derivation of the minimum 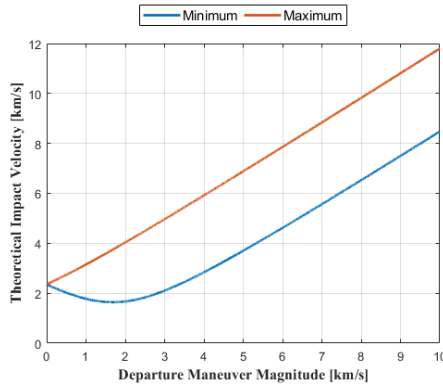and maximum impact velocities does not ensure that trajectories actually exist. The impact extrema as functions of separation maneuver magnitude appear in Figure 14. As maneuver magnitude increases, arbitrarily high impact speeds (red) are predicted. Conversely, a lower bound of approximately 1.6 km/s exists for the minimum impact speed (blue). Beyond this point, the minimum theoretical impact speed climbs with the same slope as the maximum. The slope of the increasing curves is nearly one, suggesting that a 1 km/s increase in separation maneuver magnitude corresponds to a 1 km/s increase in minimum and maximum theoretical impact speeds. This relationship demonstrates that achieving high impact velocities demands high separation maneuver magnitudes. Impact speed extrema for four maneuver magnitudes appear in Table 3. At each maneuver magnitude, the difference between the minimum and maximum impact speeds is 20 to 30 m/s. This minor variation leaves little room for impulsive trajectory design strategies that increase – or decrease – the impact speed significantly without adding additional maneuvers beyond the initial departure.

Figure 14. CR3BP minimal and maximal lunar impact speeds

Table 3. Impact speed extrema for 1, 5, 10, and 15 m/s departures

Maneuver Magnitude [m/s]	Minimum Theoretical Impact Speed [km/s]	Maximum Theoretical Impact Speed [km/s]	Minimum Observed Impact Speed [km/s]	Maximum Observed Impact Speed [km/s]
1.0	2.350	2.360	2.354	3.356
5.0	2.347	2.362	2.351	2.358
10.0	2.344	2.366	2.348	2.362
15.0	2.340	2.370	2.344	2.363

Impact Maps

To explore the observed impact velocities after NRHO departure, a set of impact maps appears in Figure 15. Impact trajectories departing from the NRHO are parameterized by the magnitude, yaw, and pitch of the separation maneuver, the location of the burn along the NRHO, and the time to impact. Finding an impacting departure trajectory requires a search through this five-dimensional search-space. The search-space is reduced to four dimensions by capping integration time at 130 days and propagating departure trajectories forward until lunar impact or departure from the lunar region. Departure from the lunar region is defined as a trajectory that crosses $x = x_{L1}$ or $x = x_{L2}$, where x_{L1} and x_{L2} represent the x components of the locations of the Earth-Moon L_1 and L_2 libration points.

As the departing trajectories are propagated forward in time, each impact trajectory is recorded along with its impact velocity, angle, location, and time of flight. The maneuvers that lead to lunar impact are plotted on the impact maps in Figure 15 colored according to the impact speed of the corresponding trajectory for maneuver magnitudes of 1, 5, and 15 m/s. Note the similarity to the yellow regions in Figure 9, indicating the consistency in results between the CR3BP and the ephemeris model. Two main structures are observed in the impact maps: rings and lobes. At lower maneuver magnitudes, rings are the dominant structures and primarily exist surrounding the anti-velocity direction at perilune; they shift as the departure location moves around the orbit. Rings represent localized maneuver directions that lead to lunar impact, and they are observed in each of the maps in Figure 15. A single ring possesses similar impact velocity characteristics throughout. At higher maneuver magnitudes, another group of rings forms around the velocity direction, characterized by higher impact velocities, again consistent across each ring. The second type of structure is observed as lobe-like patterns centered on the anti-velocity direction. At perilune, as in Figures 15b and 15c, these lobes appear as sets of concentric ring structures, but as the departure location is shifted, they deform and lose symmetry, as observed in Figure 15f. Impact velocity varies continuously across each lobe. A key feature of the lobe structures is that a small change in maneuver direction still results in an impacting trajectory; impact departure directions located on the isolated ring structures do not share this robustness. It is observed that maneuvers with a larger component in the anti-velocity direction result in lower impact speeds. Intuitively, as anti-velocity burns reduce the energy of a spacecraft, speed decreases at any particular position. Impact velocities are observed within the range bounded by the theoretical minimum observed impact speeds, as summarized in Table 3.
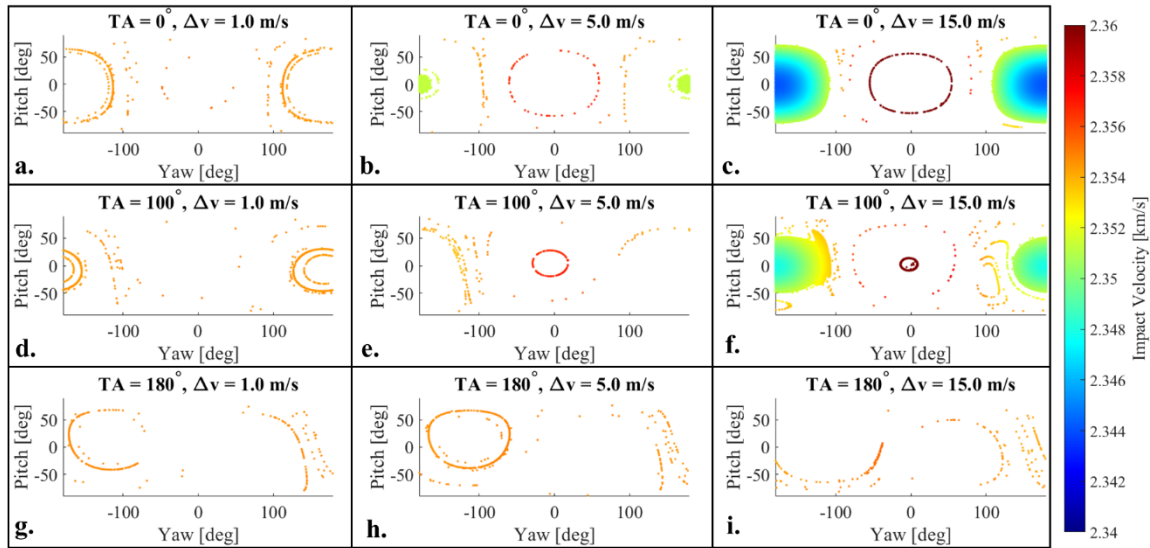

Figure 15. Impact speeds for separation maneuvers of 1, 5, and 15 m/s at various true anomalies on the ascending half of the 9:2 NRHO

In Figure 16, a series of maps is stacked with the TA of the separation burn along the vertical axis. These 3D maps are colored according to lunar impact angle for burn magnitudes of 5 and 15 m/s. Impact angle is defined as the velocity vector angle at impact with respect to the local surface normal. Thus, an angle of 0°

represents an impact normal to the surface while impact angles near 90° are tangent to the lunar surface at impact. Immediately apparent are rings or shells surrounding the velocity direction, solid lobes around the anti-velocity direction, and other structures and chaotic points throughout the maps. Consistent impact angles are absent in the ring or shell structures for any given TA across all true anomalies and maneuver magnitudes; large variation in angle exists within each single ring. Within the larger lobe structures, however, a relatively smooth gradient across impact angle is observed. Discontinuous jumps are apparent within the lobes in Figure 16b, marked by a white arrow. The cause of these discontinuities is apparent in Figure 17; Figure 17a is a map corresponding to separation at perilune. Near the anti-velocity direction, all of the transfers in the lobe are 2-revolution transfers. As the maneuver direction shifts away from the anti-velocity direction, the latitude of impact rises, and the impact angle decreases. Beyond a critical value, the trajectory does not impact the surface; rather, two more revolutions are added before impacting at a lower impact angle. An impacting trajectory prior to this discontinuity appears in Figure 17b while an impacting trajectory immediately following the discontinuity appears in Figure 17c. Note that the 4-revolution transfers proceed through the range of impact angles much more quickly than the 2-revolution transfers because of the increased sensitivity in the final states resulting from the increase in transfer time. The impact angles outside of the lobe structures are quite unpredictable and, as the departure location shifts toward apolune, this unpredictability grows. Such chaotic behavior is in contrast to the relatively predictable behavior generally observed in the impact velocity. Figures 15 and 16 demonstrate that the magnitude of spacecraft velocity at impact is easier to predict than the direction of spacecraft velocity. The chaotic nature of the region disperses trajectories in geometry, but because impact velocity is largely a function of energy in a conservative system, it remains predictable despite large variations in geometry.
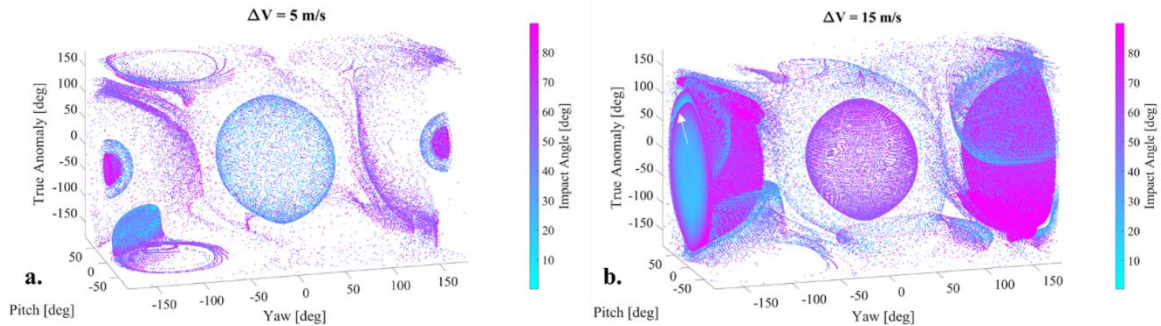

Figure 16. Impact angles for separation maneuvers of 1, 5, and 15 m/s at three true anomalies on the ascending half of the 9:2 NRHO
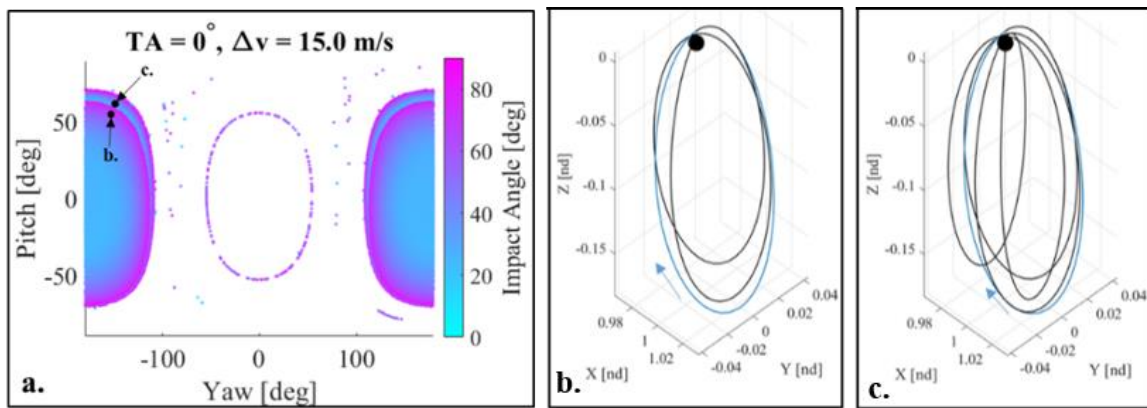

Figure 17. A 2-revolution (b) and 4-revolution (c) impact trajectory occurring inside and outside the discontinuity in the anti-velocity lobe in Figure 17(a).

The time to impact along trajectories offers an indication of transfer geometry without visual inspection of individual trajectories; for a given application, the time to impact may also rule out certain transfer geometries due to spacecraft capabilities. In Figure 18, a series of maps is again stacked with the TA of the

separation burn represented along the vertical axis. In this map, however, the points are colored according to time to impact for burn magnitudes of 5 and 15 m/s. As maneuver magnitude is increased, the time to impact tends to decrease. In both cases, the minimum time to impact is observed close to the anti-velocity direction. As with the impact speeds, the time to impact remains relatively constant throughout a ring (or shell) structure. However, in contrast to impact speed, time to impact is consistent throughout the lobes as well. A discontinuity appears in the lobe in Figure 18b, marked by a white arrow; this discontinuity corresponds to the observed jump from 2-revolution to 4-revolution impact trajectories. Figure 19 demonstrates the use of time to impact as a quantifiable measure of geometry. A single slice of the 3D map in Figure 18b appears in Figure 19a for a separation TA = 180°. Impact trajectories completing 2, 3, 4, and 5 revolutions are identified from variations in the time to impact; each trajectory corresponds to a separation burn marked on the map in Figure 19a.
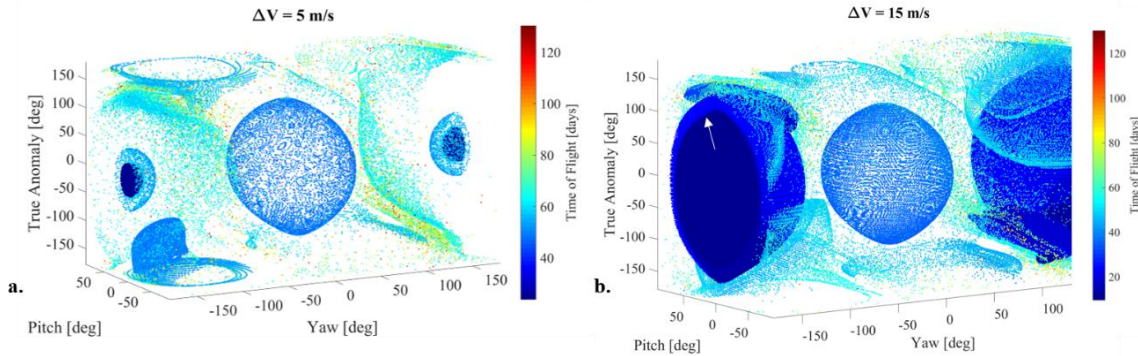

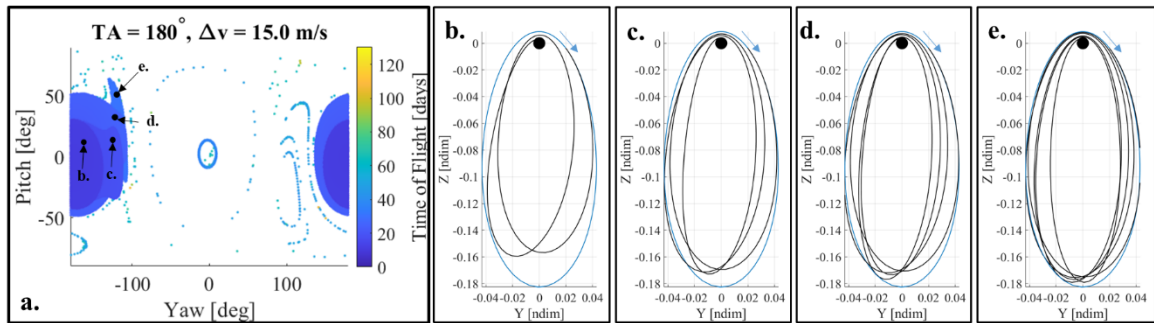**Figure 18. Times to impact for separation maneuvers of 5 and 15 m/s**

Figure 19. Differing multi-revolution transfers identifed from variations in time to impact

Maps are also used to identify maneuvers that lead to specific impact locations on the lunar surface. Defining latitude and longitude with respect to the rotating frame in the CR3BP and assuming that the Moon is exactly fixed in its tidal lock, the latitude and longitude of the impact locations are computed. Figure 20 depicts impact locations for various magnitudes and departure locations. Interestingly, the 1 m/s and 15 m/s cases show more overall structure than the 5 m/s case. The 1 m/s trajectories demonstrate that, at all depicted departure locations, transfers exist to the lunar south pole region. The 15 m/s case yields a lack of impact trajectories near the south pole with a majority of impacts occurring in the northern hemisphere. The streaks in impact location resulting from 15 m/s separation burns in Figures 20c and 20f correspond to the multi-revolution transfers depicted in Figures 17 and 19, respectively. The anti-velocity lobes, therefore, cluster not only in yaw-pitch space but also in lunar impact position. This clustering provides a level of robustness on both sides of the impact transfer. In general, at higher maneuver magnitudes, the percentage of impact trajectories in the southern hemisphere drops. In all cases, however, the impact locations outside the streaks are either part of a ring structure or are one-off impact departures in yaw-pitch space, vastly reducing their robustness. Impact locations on the lunar surface are explored in further depth in a concurrent study.[14]
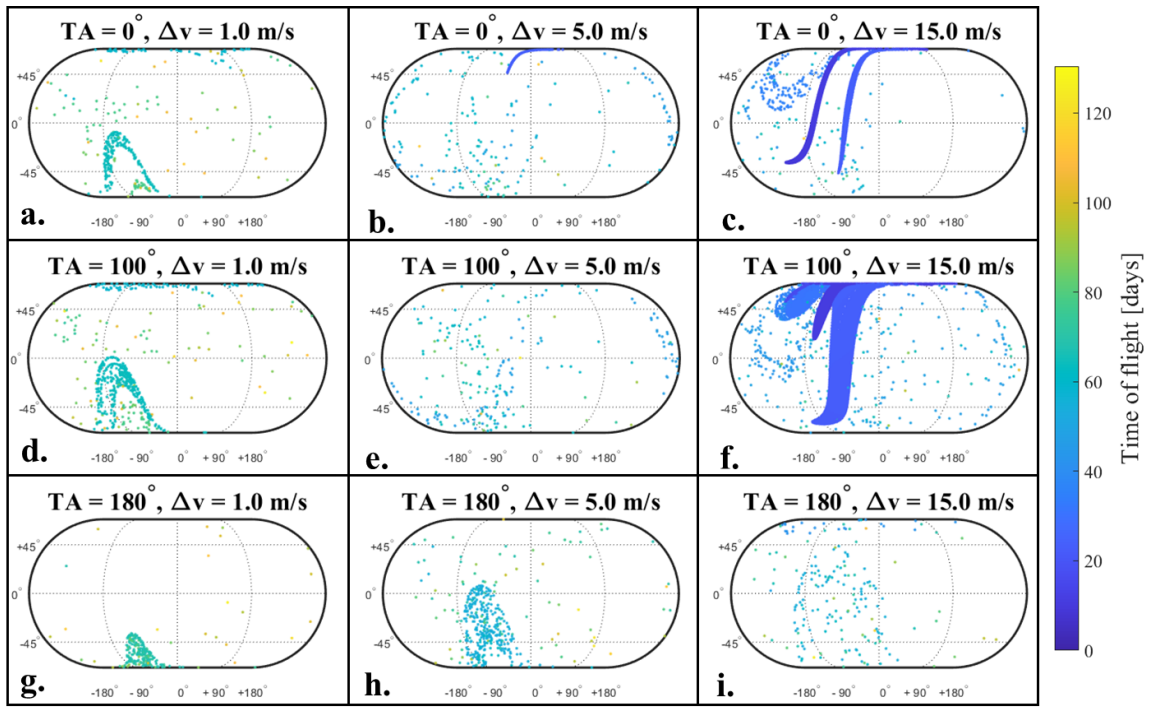
Figure 20. Impact locations on lunar surface for separation maneuvers of 1, 5, and 15 m/s at various true anomalies on the ascending half of the NRHO

Commonly Observed Geometries

Three dominant geometries arise in the impact trajectories explored in the current analysis. These geometries are summarized in Figure 21. Figure 21a represents a map relating separation burn direction to time to impact for a 15 m/s Δ𝑣 applied at apolune. Figure 21b depicts a multi-revolution transfer resulting from a burn near the anti-velocity direction; this type of geometry is responsible for the streaks observed in Figures 20c and 20f. This multi-revolution geometry is present at and above maneuver magnitudes of 5 m/s, and offers the most robust transfers in terms of the sensitivity of final impact location to error in the initial departure location and maneuver direction. An example of motion present in the ring structures surrounding velocity-direction maneuvers appears in Figure 21c. This type of geometry strongly resembles Period-4 Halo Orbits investigated by Zimovan-Spreen and Howell[15] and may be related to the manifold structures originating from the unstable members of the family. The geometry present in Figure 21d is similar to that of the unstable manifold structures in the Butterfly orbit family.[2] These types of impact trajectories originate from maneuvers outside of the lobes surrounding the anti-velocity direction. The separation burns leading to the impact trajectories in Figure 21b-d are marked by black points on the map in Figure 21a. The geometry of trajectories departing the NRHO and impacting the lunar surface appear to be closely related to the geometry of nearby periodic orbit family manifolds. Further investigation into the relationship of these structures may inform future impact trajectory design methodologies.
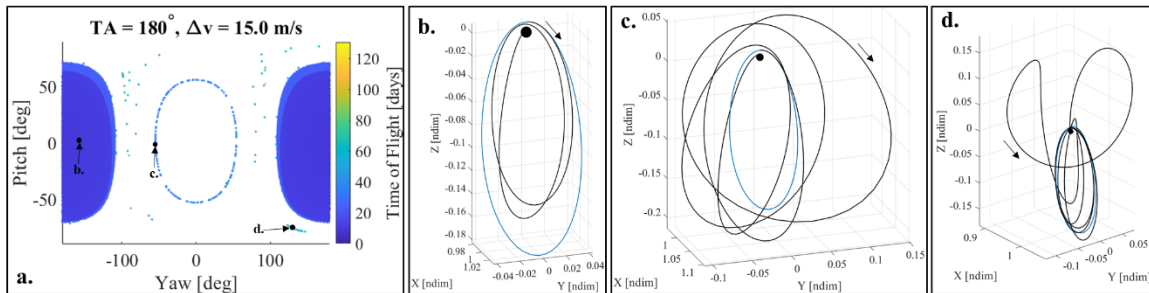

Figure 21. Commonly observed impact trajectory geometries

CONCLUDING REMARKS

Objects departing the Gateway may be destined for heliocentric space or the lunar surface. Reliable delivery to the desired destination is imperative for safe spacecraft operations. The multibody dynamical environment in cislunar space complicates trajectory design while providing opportunities for low-cost orbit transfers. The natural flow of objects in this regime is explored; although not well defined near perilune, the unstable manifold directions near apolune in the Earth-Moon CR3BP accurately describe departing behavior of trajectories originating in NRHOs.

Departures to heliocentric space require sufficient energy at NRHO departure as well as a favorable orientation in the Sun-B_1 frame. The energy at departure is not directly predicted by the magnitude of the separation burn, as the Sun-B_1 Hamiltonian is affected by the pattern of the departure flow, which in turn depends on the location, magnitude, and direction of the separation burn. Hamiltonian maps are generated that yield at a glance maneuver parameters that lead to sufficiently energetic trajectories. Then, the escape success is related to the maneuver orientation in the Sun-B_1 frame to recommend separation burns of 3.5 m/s and 15 m/s away from perilune that lead to reliable heliocentric escape in the presence of navigation and maneuver execution errors. Finally, lunar impact trajectories are explored, including the correlation of separation burn magnitude, direction, and location with lunar impact speed, angle, and location. The time of flight is an indicator of trajectory geometry.

ACKNOWLEDGMENTS

REFERENCES

[1]Gates, M., M. Barrett, J. Caram, V. Crable, D. Irimies, D. Ludban, D. Manzell, and R. Ticker, "Gateway Power and Propulsion Element Development Status," 69th International Astronautical Congress, Bremen, Germany, October 2018.

[2]Zimovan, E., K. C. Howell, and D. C. Davis, "Near Rectilinear Halo Orbits and Their Application in Cis-Lunar Space," 3rd IAA Conference on Dynamics and Control of Space Systems, Moscow, Russia, May-June 2017.

[3]Boudad, K. K., D. C. Davis, and K. C. Howell, "Disposal Trajectories From Near Rectilinear Halo Orbits," AAS/AIAA Astrodynamics Specialists Conference, Snowbird, Utah, August 2018.

[4]Davis, D.C., K.K. Boudad, and K.C. Howell, "Disposal, Deployment, and Debris in Near Rectilinear Halo Orbits," AAS/AIAA Space Flight Mechanics Meeting, Maui, Hawaii, January 2019.

[5]Szebehely, Z., *Theory of Orbits: The Restricted Problem of Three Bodies*, Academic Press, New York, 1967.

[6]Gomez, G., J. Llibre, R. Martinez, and C. Simo, *Dynamics and Mission Design near Libration Points*, Vol. 2. World Scientific, 2001.

[7]Boudad, K.K., "Disposal Dynamics from the Vicinity of Near Rectilinear Halo Orbits in the Earth-Moon-Sun System", M.S. Thesis, West Lafayette, Indiana, December 2018.

[8]Boudad, K.K., K.C. Howell, and D.C. Davis, "Near Rectilinear Halo Orbits in Cislunar Space within the Context of the Bicircular Four-Body Problem," 2nd IAA/AAS SciTech Forum, Moscow, Russia, June 25 - 27, 2019.

[9]Grebow, D., M. Ozimek, K. Howell, and D. Folta, "Multibody Orbit Architectures for Lunar South Pole Coverage," *Journal of Spacecraft and Rockets*, Vol. 45, Mar. 2008.

[10]Guzzetti, D., Zimovan, E.M., and Howell, K.C., "Stationkeeping Methodologies for Spacecraft in Lunar Near Rectilinear Halo Orbits," AAS/AIAA Spaceflights Mechanics Meeting, San Antonio, Texas, February 2017.

[11]Phillips, S.M. and D.C. Davis, "Cloud Computing Methods for Near Rectilinear Halo Orbit Trajectory Design," AAS/AIAA Astrodynamics Specialists Conference, Portland, Maine, August 2019.

[12]Newman, C. P., D. C. Davis, R. J. Whitley, J. R. Guinn, and M. S. Ryne, "Stationkeeping, Orbit Determination, and Attitude Control for Spacecraft in Near Rectilinear Halo Orbit," AAS/AIAA Astrodynamics Specialists Conference, Snowbird, Utah, August 2018.

[13]Davis, D.C., Multi-body Trajectory Design Strategies Based on Periapsis Poincaré Maps. PhD Dissertation, Purdue University, 2011.

[14]Wittal, M.M., "Spaceflight Hazards of Escape-Velocity-Domain Impact Ejecta in the CR3BP," AAS/AIAA Astrodynamics Specialists Conference, Portland, Maine, August 2019.

[15]Zimovan-Spreen, E., Howell, K. C., "Dynamical Structures Nearby NRHOs with Applications in Cislunar Space," AAS/AIAA Astrodynamics Specialists Conference, Portland, Maine, August 2019.